Atmos. Chem. Phys., 24, 3079–3091, 2024
https://doi.org/10.5194/acp-24-3079-2024

Atmospheric Chemistry and Physics
Open Access

Aqueous-phase chemistry of glyoxal with multifunctional reduced nitrogen compounds: a potential missing route for secondary brown carbon

Yuemeng Ji[1,2], Zhang Shi[1,2], Wenjian Li[1,2], Jiaxin Wang[1,2], Qiuju Shi[1,2], Yixin Li[3], Lei Gao[1,2], Ruize Ma[1,2], Weijun Lu[2], Lulu Xu[1,2], Yanpeng Gao[1,2], Guiying Li[1,2], and Taicheng An[1,2]

[1]Guangdong Key Laboratory of Environmental Catalysis and Health Risk Control, Guangdong-Hong Kong-Macao Joint Laboratory for Contaminants Exposure and Health, Institute of Environmental Health and Pollution control, Guangdong University of Technology, Guangzhou 510006, China
[2]Guangzhou Key Laboratory of Environmental Catalysis and Pollution Control, Key Laboratory of City Cluster Environmental Safety and Green Development, School of Environmental Science and Engineering, Guangdong University of Technology, Guangzhou 510006, China
[3]Department of Chemistry, University of California, Irvine, CA 92697, USA

Correspondence: Taicheng An (antc99@gdut.edu.cn)

Received: 12 November 2023 – Discussion started: 20 November 2023
Revised: 28 January 2024 – Accepted: 7 February 2024 – Published: 11 March 2024

Abstract. The aqueous-phase chemistry of glyoxal (GL) with reduced nitrogen compounds (RNCs) is a significant source for secondary brown carbon (SBrC), which is one of the largest uncertainties in climate predictions. However, a few studies have revealed that SBrC formation is affected by multifunctional RNCs, which have a non-negligible atmospheric abundance. Hence, we assessed theoretical and experimental approaches to investigate the reaction mechanisms and kinetics of the mixtures for ammonium sulfate (AS), multifunctional amine monoethanolamine (MEA), and GL. Our experiments indicate that light absorption and growth rate are enhanced more efficiently in the MEA–GL mixture relative to AS–GL and MEA–AS–GL mixtures and MEA reactions of the chromophores than in the analogous AS reactions. Quantum chemical calculations show that the formation and propagation of oligomers proceed via four-step nucleophilic addition reactions in three reaction systems. The presence of MEA provides the two extra branched chains that affect the natural charges and steric hindrance of intermediates, facilitating the formation of chromophores. Molecule dynamics simulations reveal that the interfacial and interior attraction on the aqueous aerosols with MEA is more pronounced for small α-dicarbonyls to facilitate further engagement in the aqueous-phase reactions. Our results show a possible missing source for SBrC formation on urban, regional, and global scales.

1 Introduction

Brown carbon (BrC) represents the most important source of carbonaceous aerosols, with profound implications for the global climate, air quality, and human health (Laskin et al., 2015; Marrero-Ortiz et al., 2018; Li et al., 2022; Yan et al., 2018; Yuan et al., 2023). Chemical transport models reveal that a non-negligible radiative forcing by BrC ranges from 0.05 to 0.27 $\mathrm{W\,m^{-2}}$ averaged globally (Tuccella et al., 2020; Wang et al., 2018; De Haan et al., 2020; Zhang et al., 2020; Laskin et al., 2015; Moise et al., 2015). Large differences in these estimated data result from the uncertainties of BrC on its formation mechanisms, chemical composition, and optical properties (An et al., 2019; Shi et al., 2020; Kasthuriarachchi et al., 2020; Corbin et al., 2019). This affects the understanding of the radiative effect in current climate models (Liu et al., 2020; Zhang et al., 2020, 2023). Compared with primary BrC, the sources and formation of secondary brown carbon (SBrC) are more complex and lack understanding in detail (Lin et al., 2015; Yuan et al., 2020; Srivastava et al., 2022). Hence, in recent years, great efforts have been made to better understand the chemical composition and formation mechanisms of SBrC chromophores.

There is compelling evidence that the heterogeneous reactions of reduced nitrogen compounds (RNCs) and small α-dicarbonyls have been recognized as significant sources of SBrC (Hawkins et al., 2018; De Haan et al., 2018; George et al., 2015). These SBrC chromophores are normally conjugated and are possible heteroaromatic species, such as imidazole (IML) and its derivatives (De Haan et al., 2009b, a; Yang et al., 2022). Numerous previous studies paid much attention to BrC from the secondary processes of small α-dicarbonyls with ammonium sulfate (AS) and methylamine (MA) (De Haan et al., 2020, 2019, 2009a; Lin et al., 2015). For example, nearly 30 chromophores were detected in the AS-methylglyoxal (MG) mixture by HPLC–PDA–HRMS, and nitrogen-containing compounds account for more than 70 % of the overall light absorption within the 300–500 nm range (Lin et al., 2015). Some studies have also revealed that the absorption of BrC generated in the AS–MG or MA–MG mixture increases with pH value (Hawkins et al., 2018; Sedehi et al., 2013). Also, the iminium pathway is predominant, while $\mathrm{pH} < 4$ to form IML and its derivatives is suppressed at pH 4 (Nozière et al., 2009; Sedehi et al., 2013; Yu et al., 2011). Hence, pH value has a large effect on the formation of SBrC chromophores, but the chemical mechanisms of BrC formation under the different pH values remain unclear, hindering a systematical understanding of its integrated atmospheric chemistry and non-negligible environmental impacts.

On one hand, multifunctional RNCs (such as ethanolamines and amino acids) display strong atmospheric activity in terms of the formation of SBrC with a non-neglected atmospheric concentration (Huang et al., 2016; Ge et al., 2011; Powelson et al., 2014; Trainic et al., 2012; Laskin et al., 2015; Ning et al., 2022). For example, rapid BrC formation was detected in glycine reactions with small α-dicarbonyls, and sub-micrometer amino acid particles exhibited high growth upon exposure to small α-dicarbonyls (Powelson et al., 2014; Sedehi et al., 2013; De Haan et al., 2009b; Trainic et al., 2012). On the other hand, monoethanolamine (MEA) is an amine-based solvent for post-combustion CO_2 capture (PCCC) technology with a relatively high vapor pressure, emitting 80 t per year into the atmosphere for each 1×10^6 t of CO_2 removed per year (Karl et al., 2011; Puxty et al., 2009; Shen et al., 2019). Recent field measurement has shown that MEA is the second-most abundant organic amine in $PM_{2.5}$ in Shanghai besides MA (Huang et al., 2016). However, to the best of our knowledge, few previous results are available on the participation of MEA in the SBrC formation with small alpha-dicarbonyls, and studies of its potential role in the atmosphere and human health have not been attempted.

Hence, we elucidated the chemical mechanisms of BrC chromophores from the mixtures of typical reaction of RCNs (i.e., MEA and AS) with small α-dicarbonyls using combined theoretical and experimental methods. Herein, glyoxal (GL) is selected as the representative of small α-dicarbonyls due to its high global emissions and significant contribution to BrC (Fu et al., 2008; Myriokefalitakis et al., 2008; Shi et al., 2020; Nie et al., 2022; Gomez et al., 2015). The chemical composition of the BrC chromophores was characterized by mass spectrometry at different initial pH values and the optical properties were measured using UV–Vis spectrophotometry. Possible pathways were calculated using density functional theory, and the mechanism of BrC chromophore formation was also simulated. The effects of multifunctional amine in the formation of SBrC chromophores were elaborated further. Additionally, the potential implications of multifunctional amine for climate radiative forcing were stated and discussed briefly.

2 Experimental methods and theoretical calculations

2.1 Experimental section

The procedures of each experiment are summarized in Fig. S1 in the Supplement. All reagents were used as described in the Supplement. Three mixtures were prepared under atmospheric-relevant aqueous conditions to generate SBrC: AS–GL, MEA–GL, and MEA–AS–GL. Briefly, the AS–GL (1 M) mixture was prepared by adding AS to aqueous GL (in ultrapure water) for a final concentration of 1 M of each reactant in the volumetric flasks. For the two MEA-containing mixtures, MEA was acidified with diluted sulfuric acid (20 %) to prevent GL from reacting with MEA in alkaline conditions. The acidified MEA was then combined with aqueous GL similar to that described for the AS–GL (1 M) mixture. All three solutions mentioned above were then diluted to reach a final concentration of 1 M in three 50 mL volumetric flasks. To explore the effects of pH values, the three mixtures were prepared with an initial pH value of 3 or 4 via the addition of sulfuric acid (20 %) or sodium hydroxide solution (2 M) prior to the mixing of RNCs and GL (Kampf et al., 2016; Yu et al., 2011). Each mixture was transported into brown vials, which has been proven to avoid the photolysis and light-induced reactions of light-absorbing products (Kampf et al., 2012), to guarantee efficiently produced chromophores in droplet evaporation collecting on the timescales of seconds (Zhao et al., 2015; Lee et al., 2014).

The absorption spectra of all mixtures were recorded by using a UV–Vis spectrophotometer (Agilent Cary 300, USA). All experimental solutions were diluted by a factor of 200 or 400 before each measurement to avoid saturation of the absorption peaks. The diluted samples were added into a quartz cuvette with 1 cm optical path length right away to prevent the diluted samples from photolysis. The spectra recorded between 200–500 nm are shown in Fig. 1, and the blank experiments of the GL and RNC solution were performed and are presented in Fig. S2. The absorption spectra of all sam-

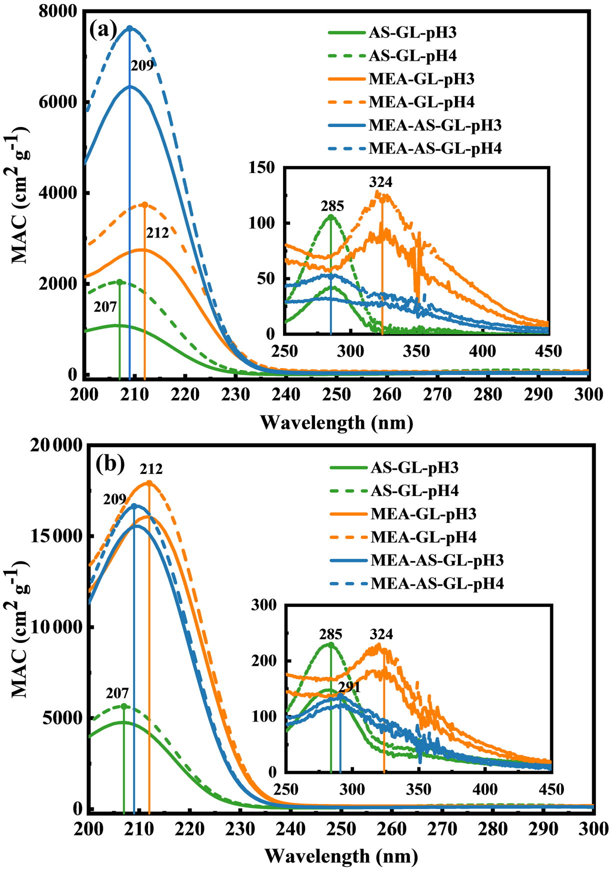

Figure 1. The MAC values for AS–GL, MEA–GL, and MEA–AS–GL mixtures at the initial pH of 3 and 4 at 1 d **(a)** and 15 d **(b)**.

ples were measured three times. The wavelength-dependent mass absorption coefficients (MACs) of experimental solutions were calculated from the initial base-10 absorbance (A_{10}) as follows:

$$\mathrm{MAC}(\lambda) = \frac{A_{10}^{\mathrm{solution}}(\lambda) \times \ln(10)}{b \times C_{\mathrm{mass}}}, \qquad (1)$$

where C_{mass} is the mass concentration of reactants and b is the path length (Aiona et al., 2017; Chen and Bond, 2010). The different dilution factors were normalized by using the MAC formula.

The samples used for mass spectrometry analysis were diluted by a factor of 800 or 1000 followed by syringe filtration. The filters were stored in brown chromatography injection vials to block the light. Ultra-performance liquid chromatography, coupled with hybrid quadrupole-exactive Orbitrap mass spectrometry (UPLC-Q-Orbitrap HRMS, Thermo Scientific™, USA) (Wang et al., 2017), was employed to obtain structural data of chromophores in this study. MS^2 analysis was used for all chromophores with a weight error of less than 10 ppm compared with the theoretical mass to obtain fragment information for the identification of structure analysis. A detailed description of the mass spectrometry and chromatographic conditions is in the Supplement.

2.2 Quantum calculations and molecular dynamics simulations

Quantum chemical calculations were performed using the Gaussian 09 package (Frisch et al., 2013). Structures for all stationary points (SPs), including reactants, intermediates, transition states (TSs), and products, were optimized using the hybrid density functional of the M06-2X method (Zhao and Truhlar, 2007) with a 6-311G(d,p) basis set, i.e., at the M06-2X/6-311G(d,p) level (Ji et al., 2017). The solvent effect was considered using the solvation model based on density (SMD) to simulate the aqueous environment (Gao et al., 2016; Marenich et al., 2009). Harmonic frequency calculation was carried out at the same level as structural optimization to verify whether an SP was a TS (with one and only imaginary frequency) or a minimum (without imaginary frequencies) (Ji et al., 2022). The intrinsic reaction coordinate calculation was performed to confirm that the TSs connected with the corresponding reactants and products. A single-point energy (SPE) calculation was executed using the M06-2X method with a more flexible 6-311+G(3df,3pd) basis set to obtain more accurate potential energy surfaces (PESs). For the pathways with TSs, the rate constants (k) were calculated via the conventional transition state theory (TST) (Evans and Polanyi, 1935; Eyring, 1935; Galano and Alvarez-Idaboy, 2009; Gao et al., 2014). To simulate real atmospheric conditions in the solution, the calculated k values were refined by solvent cage effects (Okuno, 1997) and diffusion-limited effects (Collins and Kimball, 1949), of which the calculation details of diffusion-limited rate constant k_{d} can be seen in the Supplement. For the pathways without TSs, the corresponding k values are predominated by the diffusion-limit effect, which is equal to the diffusion-limited rate constants.

The classical molecular dynamics (MD) simulation was performed using the NAMD package (Phillips et al., 2005) to simulate the heterogeneous processes of GL from gas to the AS and MEA particles. The AS particle is composed of 39 SO_4^{2-}, 78 NH_4^+, and 2046 H_2O in a box size of $40 \times 40 \times 40$ Å^3, while the MEA particle consists of 39 MEA and 2036 H_2O. The 5 ns equilibration at the time step of 1 fs was executed in the isothermal–isochoric (*NVT*) ensemble ($T = 298$ K) to ensure the thermodynamic equilibrium of particles (Shi et al., 2020; Zhang et al., 2019). The MD simulation of 2 ns is run via the NVT ensemble. MEA and GL were described using the CHARMM force field (Jorgensen et al., 1996) and H_2O was described using the TIP3P model (Martins-Costa et al., 2012). The fixed charges on NH_4^+ and SO_4^{2-} are scaled by 0.75 to account for the electronic polarizability (Leontyev and Stuchebrukhov, 2011; Mosallanejad et al., 2020). The periodic boundary conditions were selected for three dimensions. In order to calculate the kinetic trajectories of GL from gas to two target particles, the free-energy profile along the distance of the center of mass between each particle and GL was calculated via umbrella sampling (Torrie and Valleau, 1977) and the weighted-histogram analysis method (Kumar et al., 1992) based on the above equilibrated molecular dynamics trajectories. The bias potential force constant was equal to 10 kcal mol^{-1} $Å^{-2}$.

3 Results and discussion

3.1 Mass absorption coefficients of BrC chromophores

The mass absorption coefficients (MACs) identified in AS–GL, MEA–GL, and MEA–AS–GL mixtures at the initial pH of 3 and 4 (denoted as pH = 3 and pH = 4) are shown in Fig. S3. The maximum adsorption peaks are located at 207, 212, and 209 nm for AS–GL, MEA–GL, and MEA–AS–GL mixtures at pH = 3, respectively, and the corresponding location is not changed at pH = 4. The MAC values of the maximum adsorption peaks are in the range of 1080–17909 cm^2 g^{-1} for the three mixtures. In addition, each mixture has an absorption peak between 285–324 nm (Fig. S4) with a range of 42–228 cm^2 g^{-1}, which is consistent with the MAC values measured by Powelson et al. (2014) at the reaction time of 4 d but is smaller than the values measured by Zhao et al. with a long reaction time of 2–3 months (Zhao et al., 2015). The MAC values at 207–212 and 285–324 nm exhibit a similar trend (Fig. S4). Therefore, to easily compare the absorbance in the three mixtures, we focus on the adsorption peaks in the range of 207–212 nm, which exhibits an obvious variation, and the effect of the initial pH on reaction systems is also discussed in this range. The MAC values at pH = 4 are higher than those at pH = 3 for three mixtures. For example, the MAC value in the AS–GL mixture is 2037 cm^2 g^{-1} at pH = 4, which is almost 2 times higher than that at pH = 3. Hence, the initial pH values of the solution mainly affect the MAC values rather than the locations of absorption peaks.

In order to explore the influence of the initial pH values on the MAC values, a comparison of MAC values at the initial pH 3 and 4 is performed for all three mixtures (Fig. 1a). Figure 1a shows a comparison of the MAC values for all three mixtures at the initial pH of 3 and 4. The MAC values of maximum adsorption peaks increase from the AS–GL to MEA–GL to MEA–AS–GL mixture, ranging from 1080 to 6345 cm^2 g^{-1} at pH = 3 and from 2037 to 7617 cm^2 g^{-1} at pH = 4. The highest MAC value of MEA–AS–GL is explained by the different initial total concentration of reactants (see the ”Experimental methods and theoretical calculations” section) since the initial concentration of AS and MEA in the MEA–AS–GL mixture is 2 times higher than that in the MEA–GL or AS–GL mixture. In addition, the MAC value of maximum adsorption peak in the MEA–AS–GL mixture is higher than the sum of the values in the MEA–GL and AS–GL mixtures, and the location of the maximum absorption peak in the MEA–AS–GL mixture is between those in the MEA–GL and AS–GL mixtures. This implies that extra chromophores are yielded in the MEA–AS–GL mixture in addition to producing the same chromophores as AS–GL and MEA–GL mixtures.

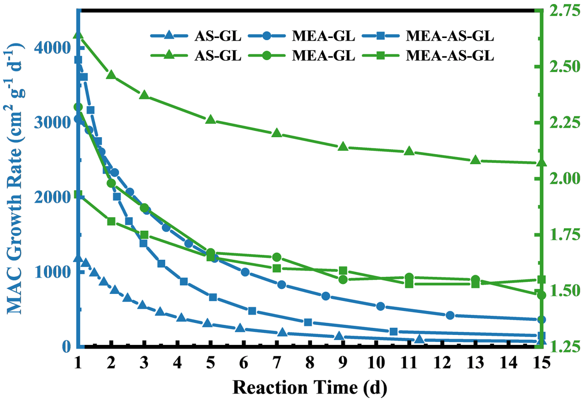

Figure 2. Dependence of the growth rates (blue line) and pH values (green line) on reaction time for AS–GL, MEA–GL, and MEA–AS–GL mixtures.

To compare the formation rate of chromophores between the different mixtures, the growth rates (GRs) of the maximum absorption peaks as a function of reaction time are shown in Fig. 2. The trend of the GR variation with reaction time at pH = 3 is similar to that at pH = 4, while the GRs of the three mixtures at pH = 4 are larger than those at pH = 3 at the beginning of the reactions. The GRs are nearly invariant after 6–9 d, implying that the chromophore formation for the three mixtures is irreversible. The MEA–AS–GL mixture exhibits larger GRs than other mixtures at the beginning of the reaction because of its higher initial concentration of reactants. As the reaction proceeds, the GRs of the MEA–GL mixture are increased and finally larger than those of other mixtures. Hence, MEA reactions form the chromophores more efficiently than the analogous AS reactions.

The GR dependence on the pH values of the three mixtures is also plotted as a function of reaction time, as shown in Fig. 2. The pH values rapidly degrade within the first 2 d in the three mixtures, which is the same trend as GRs that decrease by a factor of more than 1–3 at pH = 3 and 4. This trend is explained by ambient pH values since a known byproduct (i.e., formic acid) is formed (De Haan et al., 2009b, 2020; Galloway et al., 2009; Hamilton et al., 2013; Kampf et al., 2012; Yu et al., 2011). Note that the trend of GRs shows a decrease from the MEA–AS–GL and MEA–GL to AS–GL mixtures at the beginning of the reaction time, while the MAC values of the MEA–GL mixture are larger than those of two mixtures accompanied by the more rapid decrease in pH values in the solution after the reaction is equilibrium (Figs. 1b and 2), suggesting that chromophore formation of the three mixtures depends on the ambient pH value.

3.2 Chemical composition characterization of BrC chromophores

The chemical composition characterization of formed BrC chromophores was conducted by UPLC-Q-Orbitrap HRMS. The formulas, m/z values, characteristic fragments, and structures of chromophores and intermediates are identified based on obtained mass spectrum data in the AS–GL, MEA–GL, and MEA–AS–GL mixtures (Table S1). The corresponding MS and MS^2 spectra of chromophores and intermediates are exhibited in Figs. 3 and S8–S12. For all mixtures, imidazole (IML) compounds are identified with a characteristic peak at m/z 69.045 in the MS^2 spectra. Therefore, various IML compounds are observed based on several representative peaks at m/z 69.045, including imidazole (IML$_{\mathrm{AS}}$ and IML$_{\mathrm{MEA}}$), imidazole-2-carboxaldehyde (IC$_{\mathrm{AS}}$ and IC$_{\mathrm{MEA}}$), and their hydrated forms (HIC$_{\mathrm{AS}}$ and HIC$_{\mathrm{MEA}}$) for AS–GL and MEA–GL mixtures (Table S1, Figs. 3a–b and S8–S9). For the MEA–GL mixture, extra catenulate intermediates without IML-structure characteristics are obtained at m/z values of 102.055 and 120.065 (Table S1, Figs. 3a and S10), corresponding to $C_4H_7O_2N$ (IA$_{\mathrm{MEA}}$) and $C_4H_9O_3N$ (AHA$_{\mathrm{MEA}}$ and ID$_{\mathrm{MEA}}$) compounds, respectively. However, no catenulate intermediates in the AS–GL mixture are observed in this study because of their low concentrations and short lifetimes, although they are observed by previous studies using MS/AMS and ^{1}H nuclear magnetic resonance spectroscopy (Galloway et al., 2009; Lee et al., 2013; Yu et al., 2011). In addition, as shown in Figs. 3b and S11, some IML-based products at m/z values of 145.061, 135.066, and 193.072 were obtained in the AS–GL mixture, corresponding to hydrated N-glyoxal-substituted imidazole (HGI$_{\mathrm{AS}}$), 2,2'-biimidazole (BIM$_{\mathrm{AS}}$), and its glyoxal substituted analog (GBI$_{\mathrm{AS}}$), respectively. As discussed above, an important distinction between the AS–GL and MEA–GL mixtures is the formation of bicyclic IML products (Figs. 3a–b), indicating that the optical properties of chromophores are mainly determined by mono-imidazole compounds rather than bicyclic IML compounds.

To further explore the difference of identified products in the MEA–GL and AS–GL mixtures, possible pathways leading to the identified intermediates and chromophores are illustrated in Fig. 4 along with the reaction energies (ΔG_{r}) of all pathways calculated at the M06-2X/6-311+G(3df,3pd)//M06-2X/6-311G(d,p) level. As shown in Fig. 4, the formation and propagation of oligomers were proposed to proceed via four-step nucleophilic addition (NA) reactions. For the MEA–GL mixture, three catenulate intermediates (AHA$_{\mathrm{MEA}}$, IA$_{\mathrm{MEA}}$, and ID$_{\mathrm{MEA}}$) are successively yielded by the nucleophilic attack of MEA at the reactive carbonyl site via dehydration and hydration, with the total ΔG_{r} value of $-7.8\,\mathrm{kcal\,mol^{-1}}$ (Fig. 4a). Subsequently, two-step NA reactions between ID$_{\mathrm{MEA}}$ and MEA and between DI$_{\mathrm{MEA}}$ and GL-diol (DL), followed by protonation and dehydration, yield two intermediates (HA$_{\mathrm{MEA}}$ and PIC$_{\mathrm{MEA}}$) in sequence. Although the third NA reaction between DI$_{\mathrm{MEA}}$ and DL is endothermic ($\Delta G_{\mathrm{r}} = 12.7\,\mathrm{kcal\,mol^{-1}}$), the total ΔG_{r} value of DI$_{\mathrm{MEA}}$ formation in the MEA–GL mixture is $-18.7\,\mathrm{kcal\,mol^{-1}}$ for proceeding the NA reaction to yield PIC$_{\mathrm{MEA}}$. Similarly, the formation of PIC$_{\mathrm{AS}}$ in the AS–GL mixture is also thermodynamically feasible, with the total ΔG_{r} value of $-10.9\,\mathrm{kcal\,mol^{-1}}$. However, PIC$_{\mathrm{MEA}}$ or PIC$_{\mathrm{AS}}$ is thermodynamically unstable since there is a large exothermicity of the subsequent reaction pathway ($\Delta G_{\mathrm{r}} = -78.6$ or $-50.0\,\mathrm{kcal\,mol^{-1}}$) for proceeding cyclization leading to the formation of IC$_{\mathrm{MEA}}$ or IC$_{\mathrm{AS}}$. It should be noted that for the AS–GL mixture, the fate of IC$_{\mathrm{AS}}$ is dependent on the competition between the pathways of hydration to yield HIC$_{\mathrm{AS}}$ and NA reaction with DL to form BI$_{\mathrm{AS}}$, while for the MEA–GL mixture, there are no nucleophilic sites of IC$_{\mathrm{MEA}}$ for further oligomerization to form bicyclic IML compounds because IC$_{\mathrm{MEA}}$ is imidazolium cation. Similarly, IC$_{\mathrm{MEA}}$ also undergoes a hydration reaction to form HIC$_{\mathrm{MEA}}$ with a similar structure to HIC$_{\mathrm{AS}}$. Subsequently, HIC$_{\mathrm{AS}}$ and HIC$_{\mathrm{MEA}}$ are decomposed to yield IML$_{\mathrm{AS}}$ and IML$_{\mathrm{MEA}}$, respectively, accompanied by the formation of formic acid ($\Delta G_{\mathrm{r}} = -10.2$ and $-15.6\,\mathrm{kcal\,mol^{-1}}$), which is the reason for the decrease in pH in Sect. 3.1. However, as a reaction byproduct, formic acid hardly participates in the formation of light-absorbing products, so it has little influence on the reaction mechanisms. Current results further explain our experimental results mentioned above that higher MAC and larger GR values are observed in the MEA–GL mixture than in the AS–GL mixture.

For the MEA–AS–GL mixture, the products in AS–GL and MEA–GL mixtures are also observed (Fig. 3c). Beyond that, four extra IML compounds are also observed at m/z values of 113.071, 141.066, 159.076, and 171.076, corresponding to IML (IML$_{\mathrm{MAG}}$), imidazole-2-carboxaldehyde (IC$_{\mathrm{MAG}}$) and its hydrated form (HIC$_{\mathrm{MAG}}$), and N-glyoxal-substituted imidazole (GI$_{\mathrm{MAG}}$) (Figs. 3c and S12). An extra -C_2H_4O group exists in the geometries of the above four IML compounds relative to the products of the AL–GL mixture, indicating that there are cross-reactions between MEA and AS in the MEA–AS–GL mixture. As shown in Fig. 5, the cross-NA reaction between ID$_{\mathrm{AS}}$ and MEA or ID$_{\mathrm{MEA}}$ and AS possesses a negative ΔG_{r} value of -4.8 or $-5.4\,\mathrm{kcal\,mol^{-1}}$, followed by dehydration to form the same intermediate diimine (DI$_{\mathrm{MAG}}$). This implies that the cross-reactions in the MEA–AS–GL mixture are thermodynamically favorable. Therefore, the formation and propagation of chromophores in the MEA–AS–GL mixture also proceed via NA reactions, which is the key route for the formation of BrC chromophores.

As shown in Fig. 3c, no bicyclic IML compounds are produced in the MEA–AS–GL mixture because the precursors of bicyclic IML compound (i.e., imidazole-2-carboxaldehyde) are fully hydrated under more acidic conditions than the AS–GL mixture (see pH values in Table S2). This leads to the formation of N-glyoxal-substituted imi-

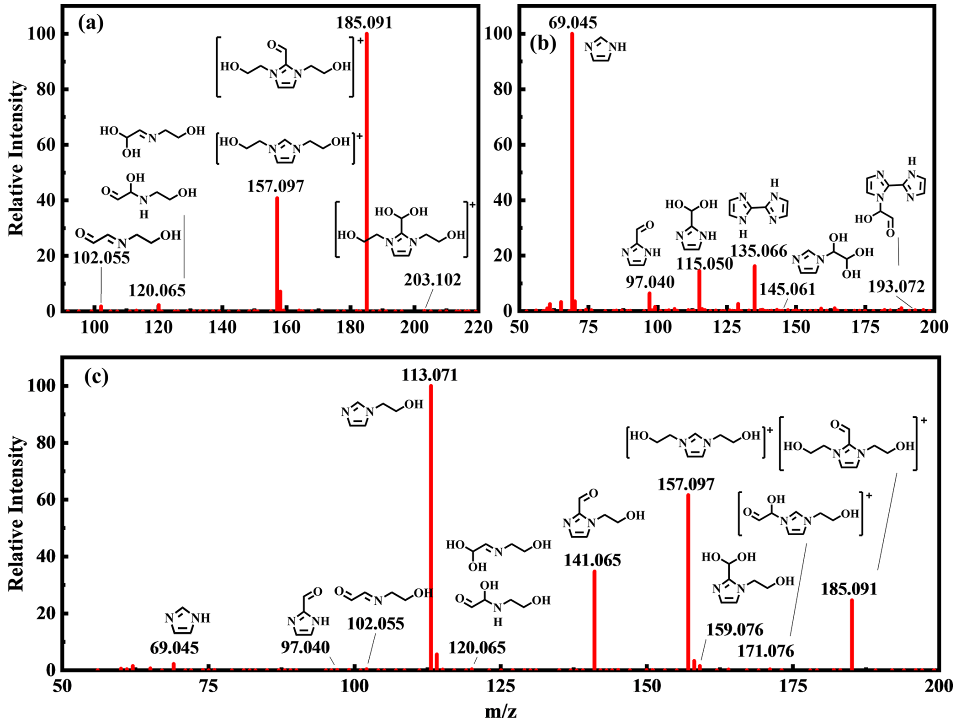

Figure 3. Mass spectra monitoring of chromophores for **(a)** MEA–GL, **(b)** AS–GL, and **(c)** MEA–AS–GL mixtures.

dazole (i.e., GI$_{\mathrm{MAG}}$) instead of bicyclic IML compounds. The similar phenomenon is also found in previous studies (Ackendorf et al., 2017; Kampf et al., 2012; Yu et al., 2011) that bicyclic IML compounds are hardly yielded from imidazole-2-carboxaldehyde in acidic conditions. As discussed above, imidazole-based structural characteristics in chromophores are maintained in the presence of MEA, but the nucleophilicity of chromophores is reduced because the nucleophilic sites are occupied. Additionally, the positively charged quaternary amine salts (such as IC$_{\mathrm{MEA}}$ and GI$_{\mathrm{MAG}}$) are also yielded in MEA–GL and MEA–AS–GL mixtures, and thereby the chemical composition and optical properties of chromophores are affected.

3.3 Chemical reaction mechanism leading to BrC chromophores

As discussed above, the four-step NA reactions are the key pathways to forming and propagating oligomers, including intermediates and chromophores for the three mixtures. Therefore, all possible pathways involved in the four key NA reactions of the three mixtures are calculated using the density functional theory. The corresponding PESs established by the M06-2X/6-311+G(3df,3pd)//M06-2X/6-311G(d,p) level are also presented in the dotted boxes of Figs. 4–5. The optimized geometries of key stationary points, including TSs, intermediates, and products, are depicted in Figs. S13–S15 at the M06-2X/6-311G(d,p) level. We first performed quantum chemistry calculation to evaluate the direct nucleophilic attack of GL by MEA or AS, which proceeds a large activation energy ($\Delta G^{\ddagger}$) value of 6.3 or 8.6 kcal mol^{-1} followed by H-shift reaction to yield AHA$_{\mathrm{MEA}}$ or AHA$_{\mathrm{AS}}$, with also a large $\Delta G^{\ddagger}$ value of 15.2 or 18.2 kcal mol^{-1} (see NA1a' and NA2a' in Fig. 4). The high $\Delta G^{\ddagger}$ values and large endothermicity of the direct NA reactions leading to AHA$_{\mathrm{MEA}}$ and AHA$_{\mathrm{AS}}$ imply that their occurrences are kinetically and thermodynamically hindered.

Hence, we explored the cationic oligomerization of chromophore formation under acidic conditions, which involves three essential steps: (1) protonation and dehydration to form cationic intermediates (CIs) or carbenium ions (CBs), (2) the nucleophilic attack of CIs or CBs by MEA and AS, and (3) the formation of intermediates and chromophores by deprotonation or dehydration. As shown in Figs. 4–5, each pathway involved in the cationic-mediated reaction mechanism proceeds without a TS, except for the deprotonation of CIs in line with the results of previous studies (Ji et al., 2020, 2022). However, the deprotonation of CIs by sulfate ion (SO_4^{2-}) possesses a negative $\Delta G^{\ddagger}$ value in this study, implying an approximate barrierless process of this kind of deprotonation.

For the first-step NA reaction (NA1a in Fig. 4) in the MEA–GL mixture, the electrophilic cationic site of CB$_{\mathrm{DL}}$ is attacked by the nucleophilic -NH$_2$ group of MEA with the ΔG_{r} value of −40.3 kcal mol^{-1}. CB$_{\mathrm{DL}}$ is broadly produced from GL and reflected from the large particle growth and formation of IML products (Ji et al., 2020; Li et al.,

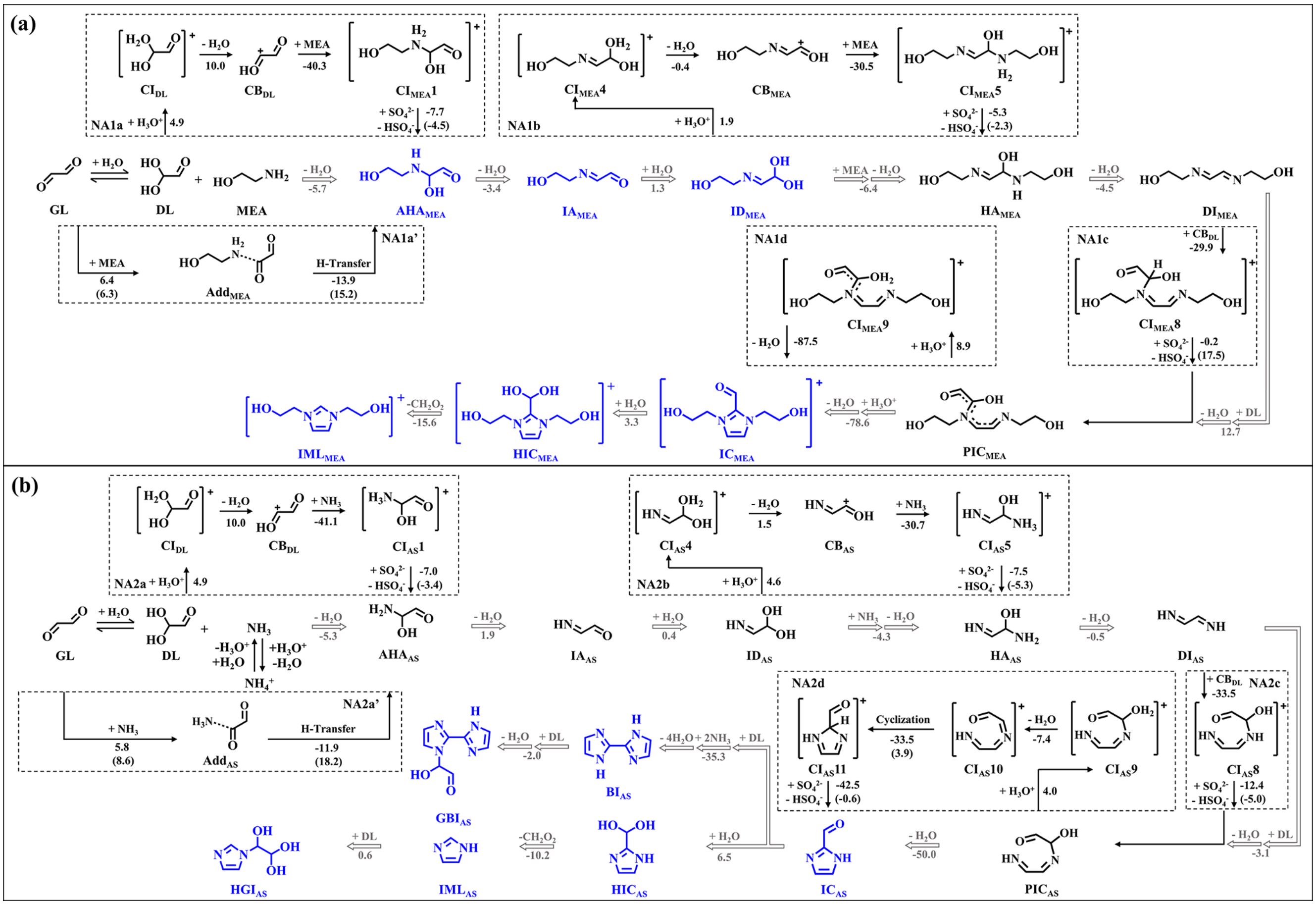

Figure 4. Possible pathways leading to chromophores for **(a)** MEA–GL and **(b)** AS–GL mixtures (oriented by gray arrows). Detailed PESs of the four NA reactions are presented in dotted boxes. The number denotes the values of ΔG_r and $\Delta G^\ddagger$ (in brackets) for each reaction step (in kcal mol^{-1}), and all energies are relative to the corresponding reactants.

2021). The deprotonation of CI$_{MEA}$1 possesses a negative $\Delta G^\ddagger$ value of -4.5 kcal mol^{-1}, and a pre-reactive complex is identified prior to the corresponding TS (detailed in the Supplement). Similarly, the other two NA1b and NA1c reactions (Fig. 4) also include protonation, dehydration, nucleophilic attack, and deprotonation to yield HA$_{MEA}$ and PIC $_{MEA}$. Kinetic data listed in Table S3 show that the rate constants of most pathways involved in the NA1a-1b and NA2a-2c reactions fall in the range of $\sim 10^9$ M^{-1} s^{-1}. Similar results can be drawn for the AS–GL mixture, suggesting that the electrostatic attraction is a significant factor to affect the NA reactions.

To further evaluate the cationic reaction mechanism, the natural bond orbital (NBO) analysis reveals that the N atom of NH_3 exhibits a more negative charge (-1.1 e) relative to MEA (-0.9 e), suggesting the stronger electrostatic attraction between CB$_{DL}$ and NH_3 to yield CI$_{AS}$1 in the first-step NA reaction (see NA1a and NA2a in Fig. 4). However, the second-step NA reaction between CB$_{MEA}$ and MEA is promoted by MEA because the presence of MEA enhances the positive charge in CB$_{MEA}$ (0.6 e), facilitating the electrostatic attraction (see NA1b and NA2b in Fig. 4). For the third-step NA reaction (see NA1c and NA2c in Fig. 4), due to the steric hindrance, the deprotonation of CI$_{MEA}$8 possesses a larger $\Delta G^\ddagger$ value relative to that of CI$_{AS}$8. Hence, the NA reactions are regulated by both the electrostatic attraction and the steric hindrance effect.

The fourth-step NA reactions in the MEA–GL and AS–GL mixtures exhibit two distinct chemical reaction mechanisms in cyclization to yield N-heterocycles (see NA1d and NA2d in Fig. 4). The protonation of PIC$_{MEA}$ and PIC$_{AS}$ occurs at the hydroxyl group to form CI$_{MEA}$9 and CI$_{AS}$9. For the MEA–GL mixture, the barrierless dehydration and cyclization of CI$_{MEA}$9 occur in one step to yield N-heterocycle (i.e., IC$_{MEA}$), with the total ΔG_r value of -78.6 kcal mol^{-1} (NA1d in Fig. 4a). However, for the AS–GL mixture, the cyclization of PIC$_{AS}$ to IC$_{AS}$ includes protonation, dehydration, cyclization, and deprotonation. Note that cyclization and deprotonation proceed via two TSs in sequence, with the corresponding $\Delta G^\ddagger$ values of 3.9 and -0.6 kcal mol^{-1}

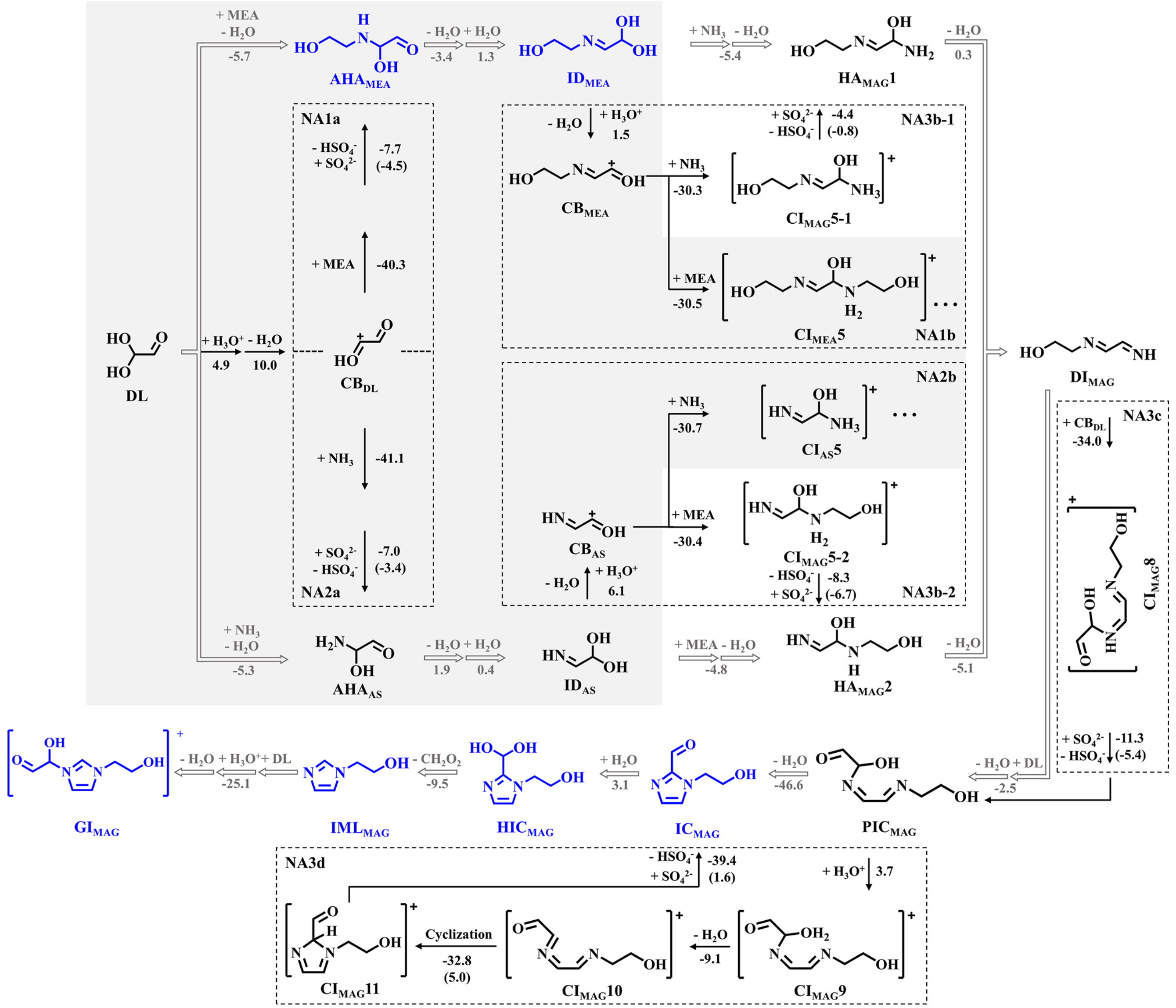

Figure 5. Possible pathways leading to chromophores for MEA–AS–GL mixture (oriented by gray arrows). Detailed PESs of the four NA reactions are presented in dotted box. The shaded area is the overlapping part with the pathways of MEA–GL and AS–GL mixtures. The number denotes the value of ΔG_r and $\Delta G^\ddagger$ (in brackets) for each reaction step (in kcal mol^{-1}), and all energies are relative to the corresponding reactants.

(NA2d in Fig. 4b), respectively, forming IC_{AS}. As discussed above, cyclization in the MEA–GL and AS–GL mixtures is the rate-limiting step to chromophore formation.

For the MEA–AS–GL mixture, $AHA_{MEA/AS}$ and $ID_{MEA/AS}$ are yielded via the same first NA reactions (NA1a/2a) as MEA–GL and AS–GL mixtures. Also, the formation of $ID_{MEA/AS}$ proceeds via protonation and dehydration to form $CB_{MEA/AS}$. However, the second NA reaction includes the cross-NA reaction of CB_{MEA} with AS (NA3b-1) or CB_{AS} with MEA (NA3b-2) to produce extra oligomers (i.e., $HA_{MAG}1$ and $HA_{MAG}2$) in contrast to MEA–GL and AS–GL mixtures. Hence, the fate of $CB_{MEA/AS}$ is dependent on the competition reaction between the pathways of self-NA reaction to form $HA_{MEA/AS}$ (NA1b/2b) and cross-NA reaction to yield $HA_{MAG}1/2$ (NA3b-1/2). The ΔG_r values of the cross-NA reactions to yield $HA_{MAG}1$ and $HA_{MAG}2$ are -30.3 and -30.4 kcal mol^{-1}, respectively, comparable with those of self-NA reactions. This suggests that both NA reactions to form HAs are equally accessible. Subsequently, $HA_{MAG}1/2$ undergoes dehydration to form DI_{MAG} and further proceeds to the third NA reaction to yield PIC_{MAG}, in line with the mechanisms of the third NA reactions for the MEA–GL and AS–GL mixtures. The cyclization of $CI_{MAG}10$ (the fourth NA reaction) possesses two successive

TSs, similar to that of the AS–GL mixture but different to that of the MEA–GL mixture. The corresponding $\Delta G^{\ddagger}$ values are obtained as 5.0 and 1.6 kcal mol^{-1}, respectively, which are larger than those of the AS–GL mixture. In summary, compared with the AS-containing mixtures, the presence of MEA provides the two extra branched chains in N atoms, which affects the natural charges and molecular steric hindrance of intermediates, to thereby facilitate the intramolecular interaction between N and C atoms to form SBrC chromophores.

4 Conclusions and atmospheric implications

BrC chromophores play an important role in the Earth's radiative balance, air quality, and human health. However, the formation mechanisms of BrC chromophores are not fully understood, hindering a comprehensive assessment of BrC chromophores on atmospheric chemistry and environmental impacts. Hence, using combined theoretical and experimental methods, we investigated the aqueous chemistry of typical RNCs with GL and evaluated the impact of typical multifunctional RNCs on the formation of BrC chromophores. Experimental studies show that the MAC values of chromophores are affected by the initial pH value for AS–GL, MEA–GL, and MEA–AS–GL mixtures and the growth rates of chromophores are enhanced in the presence of MEA. The optical properties of chromophores are regulated by monocyclic and bicyclic IML compounds in the AS–GL mixture but by monocyclic IML compounds in MEA-containing mixtures (i.e., MEA–GL and MEA–AS–GL). Combined with the results of quantum chemical calculations, chromophore formation is characterized by nucleophilic addition with large exothermicity and strong electrostatic attraction among the MEA-derived intermediates, which are also enhanced by MEA.

In addition, to simply evaluate the impacts of MEA and AS on chromosphere formation in the aqueous aerosols and fog/cloud droplets, a study of the dynamic process of GL from the gas to aqueous phase was carried out (Fig. S16). The free-energy difference reflects whether the liquid particles with MEA and AS (denoted as MEA and AS particles) prefer to adsorb and accommodate GL. As shown in Fig. S16, a larger decrease in the free energy (-3.7 kcal mol^{-1}) occurs when GL approaches the interface of the MEA particle relative to the AS particle, indicating a thermodynamically favorable process. Subsequently, the stabilized GL enters the interior region of the MEA and AS particles, with slightly endothermic reaction (1.6 and 2.4 kcal mol^{-1}). A smaller free-energy difference from the interface into the interior region of the MEA particle implies that the interfacial GL is more readily promoted to enter the interior region of the particle when the particles contain MEA compared with AS. Hence, the interfacial and interior attraction on the MEA particle is more pronounced for small α-dicarbonyls to facilitate further engagement in the aqueous-phase reactions with RNCs in the particle.

The formation of SBrC from multifunctional RNCs and small α-dicarbonyls occurs widely on aqueous aerosols and fog/cloud droplets under typical atmospheric conditions. Compared with the ubiquitous coexistence between AS and small α-dicarbonyls from global aerosol measurement, the SBrC aerosol formation from multifunctional RNC mixtures should be paid attention to during serious haze formation in China because of its atmospheric reactivities and non-negligible concentrations. Our results also imply that SBrC aerosols, if formed from the aqueous reactions between MEA and GL, likely contribute to atmospheric warming because the presence of MEA enhances the MACs of the mixture. Hence, the recognition of this aerosol formation mechanism in the radiative transfer atmospheric model is needed, representing a possible missing source for BrC formation on urban, regional, and global scales.

Data availability. All raw data can be provided by the corresponding authors upon request.

Supplement. The supplement related to this article is available online at: https://doi.org/10.5194/acp-24-3079-2024-supplement.

Author contributions. YJ and ZS designed the research; YJ, ZS, RM, and WL performed the research; YJ, ZS, WL, JW, QS, YL, LG, LX, YG, GL, and TA analyzed the data; YJ and ZS wrote the paper. YJ, YL, YG, GL, and TA reviewed and edited the paper.

Competing interests. The contact author has declared that none of the authors has any competing interests.

Acknowledgements. This work was financially supported by the National Natural Science Foundation of China (grant nos. 42077189 and 42020104001), the Guangdong Basic and Applied Basic Research Foundation (grant no. 2019B151502064), the Local Innovative and Research Teams Project of Guangdong Pearl River Talents Program (grant no. 2017BT01Z032), and the Guangdong Provincial Key R&D Program (grant no. 2022-GDUT-A0007).

Financial support. This research has been supported by the National Natural Science Foundation of China (grant nos. 42077189 and 42020104001) and the Basic and Applied Basic Research Foundation of Guangdong Province (grant no. 2019B151502064).

Review statement. This paper was edited by Qi Chen and reviewed by two anonymous referees.

References

Ackendorf, J. M., Ippolito, M. G., and Galloway, M. M.: pH Dependence of the Imidazole-2-carboxaldehyde Hydration Equilibrium: Implications for Atmospheric Light Absorbance, Environ. Sci. Technol. Lett., 4, 551–555, https://doi.org/10.1021/acs.estlett.7b00486, 2017.

Aiona, P. K., Lee, H. J., Leslie, R., Lin, P., Laskin, A., Laskin, J., and Nizkorodov, S. A.: Photochemistry of Products of the Aqueous Reaction of Methylglyoxal with Ammonium Sulfate, ACS Earth Space Chem., 1, 522–532, https://doi.org/10.1021/acsearthspacechem.7b00075, 2017.

An, Z., Huang, R. J., Zhang, R., Tie, X., Li, G., Cao, J., Zhou, W., Shi, Z., Han, Y., Gu, Z., and Ji, Y.: Severe haze in northern China: A synergy of anthropogenic emissions and atmospheric processes, P. Natl. Acad. Sci. USA, 116, 8657–8666, https://doi.org/10.1073/pnas.1900125116, 2019.

Chen, Y. and Bond, T. C.: Light absorption by organic carbon from wood combustion, Atmos. Chem. Phys., 10, 1773–1787, https://doi.org/10.5194/acp-10-1773-2010, 2010.

Collins, F. C. and Kimball, G. E.: Diffusion-controlled reaction rates, J. Colloid Sci., 4, 425–437, https://doi.org/10.1016/0095-8522(49)90023-9, 1949.

Corbin, J. C., Czech, H., Massabò, D., de Mongeot, F. B., Jakobi, G., Liu, F., Lobo, P., Mennucci, C., Mensah, A. A., Orasche, J., Pieber, S. M., Prévôt, A. S. H., Stengel, B., Tay, L. L., Zanatta, M., Zimmermann, R., El Haddad, I., and Gysel, M.: Infrared-absorbing carbonaceous tar can dominate light absorption by marine-engine exhaust, npj Clim. Atmos. Sci., 2, 12, https://doi.org/10.1038/s41612-019-0069-5, 2019.

De Haan, D. O., Tolbert, M. A., and Jimenez, J. L.: Atmospheric condensed-phase reactions of glyoxal with methylamine, Geophys. Res. Lett., 36, L11819, https://doi.org/10.1029/2009gl037441, 2009a.

De Haan, D. O., Corrigan, A. L., Smith, K. W., Stroik, D. R., Turley, J. J., Lee, F. E., Tolbert, M. A., Jimenez, J. L., Cordova, K. E., and Ferrell, G. R.: Secondary Organic Aerosol-Forming Reactions of Glyoxal with Amino Acids, Environ. Sci. Technol., 43, 2818–2824, https://doi.org/10.1021/es803534f, 2009b.

De Haan, D. O., Tapavicza, E., Riva, M., Cui, T., Surratt, J. D., Smith, A. C., Jordan, M. C., Nilakantan, S., Almodovar, M., Stewart, T. N., de Loera, A., De Haan, A. C., Cazaunau, M., Gratien, A., Pangui, E., and Doussin, J. F.: Nitrogen-Containing, Light-Absorbing Oligomers Produced in Aerosol Particles Exposed to Methylglyoxal, Photolysis, and Cloud Cycling, Environ. Sci. Technol., 52, 4061–4071, https://doi.org/10.1021/acs.est.7b06105, 2018.

De Haan, D. O., Pajunoja, A., Hawkins, L. N., Welsh, H. G., Jimenez, N. G., De Loera, A., Zauscher, M., Andretta, A. D., Joyce, B. W., De Haan, A. C., Riva, M., Cui, T., Surratt, J. D., Cazaunau, M., Formenti, P., Gratien, A., Pangui, E., and Doussin, J.-F.: Methylamine's Effects on Methylglyoxal-Containing Aerosol: Chemical, Physical, and Optical Changes, ACS Earth Space Chem., 3, 1706–1716, https://doi.org/10.1021/acsearthspacechem.9b00103, 2019.

De Haan, D. O., Hawkins, L. N., Jansen, K., Welsh, H. G., Pednekar, R., de Loera, A., Jimenez, N. G., Tolbert, M. A., Cazaunau, M., Gratien, A., Bergé, A., Pangui, E., Formenti, P., and Doussin, J.-F.: Glyoxal's impact on dry ammonium salts: fast and reversible surface aerosol browning, Atmos. Chem. Phys., 20, 9581–9590, https://doi.org/10.5194/acp-20-9581-2020, 2020.

Evans, M. G. and Polanyi, M.: Some applications of the transition state method to the calculation of reaction velocities, especially in solution, Trans. Faraday Soc., 31, 875–894, https://doi.org/10.1039/TF9353100875, 1935.

Eyring, H.: The Activated Complex in Chemical Reactions, J. Chem. Phys., 3, 107–115, https://doi.org/10.1063/1.1749604, 1935.

Frisch, M. J., Trucks, G. W., Schlegel, H. B., Scuseria, G. E., Robb, M. A., Cheeseman, J. R., Scalmani, G., Barone, V., Mennucci, B., Petersson, G. A., Nakatsuji, H., Caricato, M., Li, X., Hratchian, H. P., Izmaylov, A. F., Bloino, J., Zheng, G., Sonnenberg, J. L., Hada, M., Ehara, M., Toyota, K., Fukuda, R., Hasegawa, J., Ishida, M., Nakajima, T., Honda, Y., Kitao, O., Nakai, H., Vreven, T., Montgomery, J. A., Peralta Jr., J. E., Ogliaro, F., Bearpark, M., Heyd, J. J., Brothers, E., Kudin, K. N., Staroverov, V. N., Keith, T., Kobayashi, R., Normand, J., Raghavachari, K., Rendell, A., Burant, J. C., Iyengar, S. S., Tomasi, J., Cossi, M., Rega, N., Millam, J. M., Klene, M. Knox, J. E., Cross, J. B., Bakken, V., Adamo, C., Jaramillo, J., Gomperts, R., Stratmann, R. E., Yazyev, O., Austin, A. J., Cammi, R., Pomelli, C., Ochterski, J. W., Martin, R. L., Morokuma, K., Zakrzewski, V. G., Voth, G. A., Salvador, P., Dannenberg, J. J., Dapprich, S., Daniels, A. D., Farkas, Ö., Foresman, J. B., Ortiz, J. V., Cioslowski, J., and Fox, D. J.: Gaussian09, Revision D.01, Gaussian, Inc., Wallingford CT., USA, 2009.

Fu, T.-M., Jacob, D. J., Wittrock, F., Burrows, J. P., Vrekoussis, M., and Henze, D. K.: Global budgets of atmospheric glyoxal and methylglyoxal, and implications for formation of secondary organic aerosols, J. Geophys. Res., 113, D15303, https://doi.org/10.1029/2007jd009505, 2008.

Galano, A. and Alvarez-Idaboy, J. R.: Guanosine + OH Radical Reaction in Aqueous Solution: A Reinterpretation of the UV-vis Data Based on Thermodynamic and Kinetic Calculations, Org. Lett., 11, 5114–5117, https://doi.org/10.1021/ol901862h, 2009.

Galloway, M. M., Chhabra, P. S., Chan, A. W. H., Surratt, J. D., Flagan, R. C., Seinfeld, J. H., and Keutsch, F. N.: Glyoxal uptake on ammonium sulphate seed aerosol: reaction products and reversibility of uptake under dark and irradiated conditions, Atmos. Chem. Phys., 9, 3331–3345, https://doi.org/10.5194/acp-9-3331-2009, 2009.

Gao, Y., Ji, Y., Li, G., and An, T.: Mechanism, kinetics and toxicity assessment of OH-initiated transformation of triclosan in aquatic environments, Water Res., 49, 360–370, https://doi.org/10.1016/j.watres.2013.10.027, 2014.

Gao, Y., Ji, Y., Li, G., Mai, B., and An, T.: Bioaccumulation and ecotoxicity increase during indirect photochemical transformation of polycyclic musk tonalide: A modeling study, Water Res., 105, 47–55, https://doi.org/10.1016/j.watres.2016.08.055, 2016.

Ge, X., Wexler, A. S., and Clegg, S. L.: Atmospheric amines – Part I. A review, Atmos. Environ., 45, 524–546, https://doi.org/10.1016/j.atmosenv.2010.10.012, 2011.

George, C., Ammann, M., D'Anna, B., Donaldson, D. J., and Nizkorodov, S. A.: Heterogeneous photochemistry in the atmosphere, Chem. Rev., 115, 4218–4258, https://doi.org/10.1021/cr500648z, 2015.

Gomez, M. E., Lin, Y., Guo, S., and Zhang, R.: Heterogeneous Chemistry of Glyoxal on Acidic Solutions. An Oligomerization Pathway for Secondary Organic Aerosol Formation, J. Phys. Chem. A, 119, 4457–4463, https://doi.org/10.1021/jp509916r, 2015.

Hamilton, J. F., Baeza-Romero, M. T., Finessi, E., Rickard, A. R., Healy, R. M., Peppe, S., Adams, T. J., Daniels, M. J. S., Ball, S. M., Goodall, I. C. A., Monks, P. S., Borrás, E., and Muñoz, A.: Online and offline mass spectrometric study of the impact of oxidation and ageing on glyoxal chemistry and uptake onto ammonium sulfate aerosols, Faraday Discuss., 165, 447–472, https://doi.org/10.1039/c3fd00051f, 2013.

Hawkins, L. N., Welsh, H. G., and Alexander, M. V.: Evidence for pyrazine-based chromophores in cloud water mimics containing methylglyoxal and ammonium sulfate, Atmos. Chem. Phys., 18, 12413–12431, https://doi.org/10.5194/acp-18-12413-2018, 2018.

Huang, X., Deng, C., Zhuang, G., Lin, J., and Xiao, M.: Quantitative analysis of aliphatic amines in urban aerosols based on online derivatization and high performance liquid chromatography, Environ. Sci.-Proc. Imp., 18, 796–801, https://doi.org/10.1039/c6em00197a, 2016.

Ji, Y., Zhao, J., Terazono, H., Misawa, K., Levitt, N. P., Li, Y., Lin, Y., Peng, J., Wang, Y., Duan, L., Pan, B., Zhang, F., Feng, X., An, T., Marrero-Ortiz, W., Secrest, J., Zhang, A. L., Shibuya, K., Molina, M. J., and Zhang, R.: Reassessing the atmospheric oxidation mechanism of toluene, P. Natl. Acad. Sci. USA, 114, 8169, https://doi.org/10.1073/pnas.1705463114, 2017.

Ji, Y., Shi, Q., Li, Y., An, T., Zheng, J., Peng, J., Gao, Y., Chen, J., Li, G., Wang, Y., Zhang, F., Zhang, A. L., Zhao, J., Molina, M. J., and Zhang, R.: Carbenium ion-mediated oligomerization of methylglyoxal for secondary organic aerosol formation, P. Natl. Acad. Sci. USA, 117, 13294–13299, https://doi.org/10.1073/pnas.1912235117, 2020.

Ji, Y., Shi, Q., Ma, X., Gao, L., Wang, J., Li, Y., Gao, Y., Li, G., Zhang, R., and An, T.: Elucidating the critical oligomeric steps in secondary organic aerosol and brown carbon formation, Atmos. Chem. Phys., 22, 7259–7271, https://doi.org/10.5194/acp-22-7259-2022, 2022.

Jorgensen, W. L., Maxwell, D. S., and Tirado-Rives, J.: Development and Testing of the OPLS All-Atom Force Field on Conformational Energetics and Properties of Organic Liquids, J. Am. Chem. Soc., 118, 11225–11236, https://doi.org/10.1021/ja9621760, 1996.

Kampf, C. J., Jakob, R., and Hoffmann, T.: Identification and characterization of aging products in the glyoxal/ammonium sulfate system – implications for light-absorbing material in atmospheric aerosols, Atmos. Chem. Phys., 12, 6323–6333, https://doi.org/10.5194/acp-12-6323-2012, 2012.

Kampf, C. J., Filippi, A., Zuth, C., Hoffmann, T., and Opatz, T.: Secondary brown carbon formation via the dicarbonyl imine pathway: nitrogen heterocycle formation and synergistic effects, Phys. Chem. Chem. Phys., 18, 18353–18364, https://doi.org/10.1039/c6cp03029g, 2016.

Karl, M., Wright, R. F., Berglen, T. F., and Denby, B.: Worst case scenario study to assess the environmental impact of amine emissions from a CO_2 capture plant, Int. J. Greenh. Gas Control, 5, 439–447, https://doi.org/10.1016/j.ijggc.2010.11.001, 2011.

Kasthuriarachchi, N. Y., Rivellini, L. H., Adam, M. G., and Lee, A. K. Y.: Light Absorbing Properties of Primary and Secondary Brown Carbon in a Tropical Urban Environment, Environ. Sci. Technol., 54, 10808–10819, https://doi.org/10.1021/acs.est.0c02414, 2020.

Kumar, S., Rosenberg, J. M., Bouzida, D., Swendsen, R. H., and Kollman, P. A.: The weighted histogram analysis method for free-energy calculations on biomolecules. I. The method, J. Comput. Chem., 13, 1011–1021, https://doi.org/10.1002/jcc.540130812, 1992.

Laskin, A., Laskin, J., and Nizkorodov, S. A.: Chemistry of atmospheric brown carbon, Chem. Rev., 115, 4335–4382, https://doi.org/10.1021/cr5006167, 2015.

Lee, A. K. Y., Zhao, R., Li, R., Liggio, J., Li, S.-M., and Abbatt, J. P. D.: Formation of Light Absorbing Organo-Nitrogen Species from Evaporation of Droplets Containing Glyoxal and Ammonium Sulfate, Environ. Sci. Technol., 47, 12819–12826, https://doi.org/10.1021/es402687w, 2013.

Lee, H. J., Aiona, P. K., Laskin, A., Laskin, J., and Nizkorodov, S. A.: Effect of solar radiation on the optical properties and molecular composition of laboratory proxies of atmospheric brown carbon, Environ. Sci. Technol., 48, 10217–10226, https://doi.org/10.1021/es502515r, 2014.

Leontyev, I. and Stuchebrukhov, A.: Accounting for electronic polarization in non-polarizable force fields, Phys. Chem. Chem. Phys., 13, 2613–2626, https://doi.org/10.1039/c0cp01971b, 2011.

Li, X., Sun, N., Jin, Q., Zhao, Z., Wang, L., Wang, Q., Gu, X., Li, Y., and Liu, X.: Light absorption properties of black and brown carbon in winter over the North China Plain: Impacts of regional biomass burning, Atmos. Environ., 278, 119100, https://doi.org/10.1016/j.atmosenv.2022.119100, 2022.

Li, Y., Ji, Y., Zhao, J., Wang, Y., Shi, Q., Peng, J., Wang, Y., Wang, C., Zhang, F., Wang, Y., Seinfeld, J. H., and Zhang, R.: Unexpected Oligomerization of Small alpha-Dicarbonyls for Secondary Organic Aerosol and Brown Carbon Formation, Environ. Sci. Technol., 55, 4430–4439, https://doi.org/10.1021/acs.est.0c08066, 2021.

Lin, P., Laskin, J., Nizkorodov, S. A., and Laskin, A.: Revealing Brown Carbon Chromophores Produced in Reactions of Methylglyoxal with Ammonium Sulfate, Environ. Sci. Technol., 49, 14257–14266, https://doi.org/10.1021/acs.est.5b03608, 2015.

Liu, D., He, C., Schwarz, J. P., and Wang, X.: Lifecycle of light-absorbing carbonaceous aerosols in the atmosphere, npj Clim. Atmos. Sci., 3, 40, https://doi.org/10.1038/s41612-020-00145-8, 2020.

Marenich, A. V., Cramer, C. J., and Truhlar, D. G.: Universal Solvation Model Based on Solute Electron Density and on a Continuum Model of the Solvent Defined by the Bulk Dielectric Constant and Atomic Surface Tensions, J. Phys. Chem. B, 113, 6378–6396, https://doi.org/10.1021/jp810292n, 2009.

Marrero-Ortiz, W., Hu, M., Du, Z., Ji, Y., Wang, Y., Guo, S., Lin, Y., Gomez-Hermandez, M., Peng, J., Li, Y., Secrest, J., Zamora, M. L., Wang, Y., An, T., and Zhang, R.: Formation and Optical Properties of Brown Carbon from Small α-Dicarbonyls and Amines, Environ. Sci. Technol., 53, 117–126, https://doi.org/10.1021/acs.est.8b03995, 2018.

Martins-Costa, M. T., Anglada, J. M., Francisco, J. S., and Ruiz-Lopez, M. F.: Reactivity of volatile organic compounds at the surface of a water droplet, J. Am. Chem. Soc., 134, 11821–11827, https://doi.org/10.1021/ja304971e, 2012.

Moise, T., Flores, J. M., and Rudich, Y.: Optical properties of secondary organic aerosols and their changes by chemical processes, Chem. Rev., 115, 4400–4439, https://doi.org/10.1021/cr5005259, 2015.

Mosallanejad, S., Oluwoye, I., Altarawneh, M., Gore, J., and Dlugogorski, B. Z.: Interfacial and bulk properties of concentrated solutions of ammonium nitrate, Phys. Chem. Chem. Phys., 22, 27698–27712, https://doi.org/10.1039/d0cp04874g, 2020.

Myriokefalitakis, S., Vrekoussis, M., Tsigaridis, K., Wittrock, F., Richter, A., Brühl, C., Volkamer, R., Burrows, J. P., and Kanakidou, M.: The influence of natural and anthropogenic secondary sources on the glyoxal global distribution, Atmos. Chem. Phys., 8, 4965–4981, https://doi.org/10.5194/acp-8-4965-2008, 2008.

Nie, W., Yan, C., Huang, D. D., Wang, Z., Liu, Y., Qiao, X., Guo, Y., Tian, L., Zheng, P., Xu, Z., Li, Y., Xu, Z., Qi, X., Sun, P., Wang, J., Zheng, F., Li, X., Yin, R., Dallenbach, K. R., Bianchi, F., Petäjä, T., Zhang, Y., Wang, M., Schervish, M., Wang, S., Qiao, L., Wang, Q., Zhou, M., Wang, H., Yu, C., Yao, D., Guo, H., Ye, P., Lee, S., Li, Y. J., Liu, Y., Chi, X., Kerminen, V.-M., Ehn, M., Donahue, N. M., Wang, T., Huang, C., Kulmala, M., Worsnop, D., Jiang, J., and Ding, A.: Secondary organic aerosol formed by condensing anthropogenic vapours over China's megacities, Nat. Geosci., 15, 255–261, https://doi.org/10.1038/s41561-022-00922-5, 2022.

Ning, A., Liu, L., Zhang, S., Yu, F., Du, L., Ge, M., and Zhang, X.: The critical role of dimethylamine in the rapid formation of iodic acid particles in marine areas, npj Clim. Atmos. Sci., 5, 92, https://doi.org/10.1038/s41612-022-00316-9, 2022.

Nozière, B., Dziedzic, P., and Córdova, A.: Products and Kinetics of the Liquid-Phase Reaction of Glyoxal Catalyzed by Ammonium Ions (NH_4^+), J. Phys. Chem. A, 113, 231–237, https://doi.org/10.1021/jp8078293, 2009.

Okuno, Y.: Theoretical Investigation of the Mechanism of the Baeyer-Villiger Reaction in Nonpolar Solvents, Chem.-Eur. J., 3, 212–218, https://doi.org/10.1002/chem.19970030208, 1997.

Phillips, J. C., Braun, R., Wang, W., Gumbart, J., Tajkhorshid, E., Villa, E., Chipot, C., Skeel, R. D., Kale, L., and Schulten, K.: Scalable molecular dynamics with NAMD, J. Comput. Chem., 26, 1781–1802, https://doi.org/10.1002/jcc.20289, 2005.

Powelson, M. H., Espelien, B. M., Hawkins, L. N., Galloway, M. M., and De Haan, D. O.: Brown Carbon Formation by Aqueous-Phase Carbonyl Compound Reactions with Amines and Ammonium Sulfate, Environ. Sci. Technol., 48, 985–993, https://doi.org/10.1021/es4038325, 2014.

Puxty, G., Rowland, R., Allport, A., Yang, Q., Bown, M., Burns, R., Maeder, M., and Attalla, M.: Carbon Dioxide Postcombustion Capture: A Novel Screening Study of the Carbon Dioxide Absorption Performance of 76 Amines, Environ. Sci. Technol., 43, 6427–6433, https://doi.org/10.1021/es901376a, 2009.

Sedehi, N., Takano, H., Blasic, V. A., Sullivan, K. A., and De Haan, D. O.: Temperature- and pH-dependent aqueous-phase kinetics of the reactions of glyoxal and methylglyoxal with atmospheric amines and ammonium sulfate, Atmos. Environ., 77, 656–663, https://doi.org/10.1016/j.atmosenv.2013.05.070, 2013.

Shen, J., Xie, H.-B., Elm, J., Ma, F., Chen, J., and Vehkamäki, H.: Methanesulfonic Acid-driven New Particle Formation Enhanced by Monoethanolamine: A Computational Study, Environ. Sci. Technol., 53, 14387–14397, https://doi.org/10.1021/acs.est.9b05306, 2019.

Shi, Q., Zhang, W., Ji, Y., Wang, J., Qin, D., Chen, J., Gao, Y., Li, G., and An, T.: Enhanced uptake of glyoxal at the acidic nanoparticle interface: implications for secondary organic aerosol formation, Environ. Sci.-Nano, 7, 1126–1135, https://doi.org/10.1039/d0en00016g, 2020.

Srivastava, D., Vu, T. V., Tong, S., Shi, Z., and Harrison, R. M.: Formation of secondary organic aerosols from anthropogenic precursors in laboratory studies, npj Clim. Atmos. Sci., 5, 22, https://doi.org/10.1038/s41612-022-00238-6, 2022.

Torrie, G. M. and Valleau, J. P.: Nonphysical sampling distributions in Monte Carlo free-energy estimation: Umbrella sampling, J. Comput. Phys., 23, 187–199, https://doi.org/10.1016/0021-9991(77)90121-8, 1977.

Trainic, M., Riziq, A. A., Lavi, A., and Rudich, Y.: Role of interfacial water in the heterogeneous uptake of glyoxal by mixed glycine and ammonium sulfate aerosols, J. Phys. Chem. A, 116, 5948–5957, https://doi.org/10.1021/jp2104837, 2012.

Tuccella, P., Curci, G., Pitari, G., Lee, S., and Jo, D. S.: Direct Radiative Effect of Absorbing Aerosols: Sensitivity to Mixing State, Brown Carbon, and Soil Dust Refractive Index and Shape, J. Geophys. Res.-Atmos., 125, e2019JD030967, https://doi.org/10.1029/2019jd030967, 2020.

Wang, X., Hayeck, N., Brüggemann, M., Yao, L., Chen, H., Zhang, C., Emmelin, C., Chen, J., George, C., and Wang, L.: Chemical Characteristics of Organic Aerosols in Shanghai: A Study by Ultrahigh-Performance Liquid Chromatography Coupled With Orbitrap Mass Spectrometry, J. Geophys. Res.-Atmos., 122, 11703–11722, https://doi.org/10.1002/2017jd026930, 2017.

Wang, X., Heald, C. L., Liu, J., Weber, R. J., Campuzano-Jost, P., Jimenez, J. L., Schwarz, J. P., and Perring, A. E.: Exploring the observational constraints on the simulation of brown carbon, Atmos. Chem. Phys., 18, 635–653, https://doi.org/10.5194/acp-18-635-2018, 2018.

Yan, J., Wang, X., Gong, P., Wang, C., and Cong, Z.: Review of brown carbon aerosols: Recent progress and perspectives, Sci. Total Environ., 634, 1475–1485, https://doi.org/10.1016/j.scitotenv.2018.04.083, 2018.

Yang, Z., Tsona, N. T., George, C., and Du, L.: Nitrogen-Containing Compounds Enhance Light Absorption of Aromatic-Derived Brown Carbon, Environ. Sci. Technol., 56, 4005–4016, https://doi.org/10.1021/acs.est.1c08794, 2022.

Yu, G., Bayer, A. R., Galloway, M. M., Korshavn, K. J., Fry, C. G., and Keutsch, F. N.: Glyoxal in aqueous ammonium sulfate solutions: products, kinetics and hydration effects, Environ. Sci. Technol., 45, 6336–6342, https://doi.org/10.1021/es200989n, 2011.

Yuan, W., Huang, R.-J., Yang, L., Guo, J., Chen, Z., Duan, J., Wang, T., Ni, H., Han, Y., Li, Y., Chen, Q., Chen, Y., Hoffmann, T., and O'Dowd, C.: Characterization of the light-absorbing properties, chromophore composition and sources of brown carbon aerosol in Xi'an, northwestern China, Atmos. Chem. Phys., 20, 5129–5144, https://doi.org/10.5194/acp-20-5129-2020, 2020.

Yuan, W., Huang, R.-J., Shen, J., Wang, K., Yang, L., Wang, T., Gong, Y., Cao, W., Guo, J., Ni, H., Duan, J., and Hoffmann, T.: More water-soluble brown carbon after the residential "coal-to-gas" conversion measure in urban Beijing, npj Clim. Atmos. Sci., 6, 20, https://doi.org/10.1038/s41612-023-00355-w, 2023.

Zhang, A., Wang, Y., Zhang, Y., Weber, R. J., Song, Y., Ke, Z., and Zou, Y.: Modeling the global radiative effect of brown carbon: a potentially larger heating source in the tropical free troposphere than black carbon, Atmos. Chem. Phys., 20, 1901–1920, https://doi.org/10.5194/acp-20-1901-2020, 2020.

Zhang, W., Ji, Y., Li, G., Shi, Q., and An, T.: The heterogeneous reaction of dimethylamine/ammonia with sulfuric acid to promote the growth of atmospheric nanoparticles, Environ. Sci.-Nano, 6, 2767–2776, https://doi.org/10.1039/c9en00619b, 2019.

Zhang, X., Tong, S., Jia, C., Zhang, W., Wang, Z., Tang, G., Hu, B., Liu, Z., Wang, L., Zhao, P., Pan, Y., and Ge, M.: Elucidating HONO formation mechanism and its essential contribution to OH during haze events, npj Clim. Atmos. Sci., 6, 55, https://doi.org/10.1038/s41612-023-00371-w, 2023.

Zhao, R., Lee, A. K. Y., Huang, L., Li, X., Yang, F., and Abbatt, J. P. D.: Photochemical processing of aqueous atmospheric brown carbon, Atmos. Chem. Phys., 15, 6087–6100, https://doi.org/10.5194/acp-15-6087-2015, 2015.

Zhao, Y. and Truhlar, D. G.: The M06 suite of density functionals for main group thermochemistry, thermochemical kinetics, noncovalent interactions, excited states, and transition elements: two new functionals and systematic testing of four M06-class functionals and 12 other functionals, Theor. Chem. Acc., 120, 215–241, https://doi.org/10.1007/s00214-007-0310-x, 2007.